Article

Elastostatic Stiffness Modeling and Performance Evaluation of a 2UPR–2PRU Redundantly Actuated Parallel Manipulator

Xinxue Chai [1,2], Wei Ye [1], Qinchuan Li [1] and Lingmin Xu [1,2,*]

1   School of Mechanical Engineering, Zhejiang Sci-Tech University, Hangzhou 310018, China
2   State Key Laboratory of Mechanical System and Vibration, School of Mechanical Engineering, Shanghai Jiao Tong University, Shanghai 200240, China
*   Correspondence: lmxu93@sjtu.edu.cn

Abstract: Redundantly actuated parallel manipulators (PMs) have attracted a great deal of attention since they generally have better stiffness than non-redundantly actuated ones. This paper presents an analytical elastostatic stiffness modeling and performance study of a 2UPR–2PRU PM with actuation redundancy, which has two rotational and one translational degrees of freedom (U: universal joint; P: prismatic joint; R: revolute joint). First, the inverse displacement is reviewed and verified briefly. Second, the stiffness matrices of UPR and PRU limbs are deduced by using the principle of strain energy, followed by the overall stiffness matrix of the 2UPR–2PRU PM. Combined with the ANSYS software, the finite element analysis method is then used to verify the correctness and universality of the stiffness models by calculating the deformations of four selected configurations. Finally, the stiffness index based on the virtual work is used to evaluate the performance of the 2UPR–2PRU PM, and the influence of different external loads and operational heights on the stiffness performance is discussed. The relationship between singular configurations and the stiffness index is also presented. The stiffness models and performance distributions of the 2UPR–2PRU PM with actuation redundancy can provide references for the actual applications.

Keywords: parallel manipulator; actuation redundancy; elastostatic stiffness modeling; performance evaluation

1. Introduction

Compared with the parallel manipulators (PMs) without actuation redundancy, the redundantly actuated PMs have some advantages, such as higher stiffness and fewer singular configurations [1–3], and thus they are suitable for applications requiring high accuracy. In general, the methods for producing redundantly actuated PMs can be divided into two categories [4]: one is to replace some passive kinematic joints in the limbs with the actuated ones, and the other is to add one or more actuated limbs to the original PM, but the characteristics of the output motion stay the same. Because of the advantages of the second type with better force distributions [5,6], this paper focuses on the redundantly actuated PMs with more limbs.

Elastostatic stiffness modeling and the performance evaluation of the PMs with actuation redundancy are necessary for the design stage. The goal of the elastostatic stiffness modeling of PMs is to create a mapping between the deformations of the moving platform and the external loads in the reachable workspace [7]. The stiffness characteristics can be obtained from the stiffness matrices of all the components and PM. Many works on the stiffness modeling of PMs have been carried out, which can be mainly divided into two types: finite element analysis (FEA) [8–12], and analytical modeling [13–31]. Some scholars, such as Fauroux et al. [9–11] and Klimchik et al. [12], have adopted the FEA method to conduct some stiffness analysis. Based on the FEA method, the deformation information of corresponding configurations can be obtained directly by using some FEA

software, such as ANSYS. However, it should be noted that the deformation of different configurations can only be calculated sequentially, and the process is time-consuming [13,14]. Regarding analytical modeling, a great deal of research has been conducted by scholars such as Gosselin [16], Zhang et al. [17–19], Lipkin et al. [20], Kumar et al. [21–23], Pashkevich et al. [13], Portman et al. [26,27], Ding et al. [29], and so on. Considering the compliance of actuated joints, Gosselin [16] developed the mapping relationship between the forces and deformations of PMs. Zhang et al. [17–19] considered the compliance of the actuated joints and links and analyzed the stiffness of PMs. Lipkin et al. [20] analyzed the stiffness of the compliant system with some external loads and obtained the asymmetric stiffness matrix. Pashkevich et al. [13] investigated the overconstrained PMs with compliant actuated joints and flexible links and obtained a relatively accurate stiffness matrix. Based on the Lie-group theory and screw theory, Ding and his co-workers [29] developed a theoretical method to analyze the accuracy of the redundantly actuated and overconstrained PMs that takes the actuated errors and internal elastic forces into account. In addition to the above work, researchers have also carried out many explorations into the theoretical stiffness modeling of PMs.

This paper presents a systematic elastostatic stiffness modeling and performance analysis of a redundantly actuated 2UPR–2PRU PM [32]. The 2UPR–2PRU PM with actuation redundancy is a PM with two rotational and one translational degrees of freedom (DoFs), which has potential for the machining of curved workpieces with high precision. In this paper, the analytical stiffness modeling method based on the strain energy [33,34] is used. The elastostatic stiffness matrices of limbs and the overall PM can be easily developed by utilizing the principle of strain energy. All the results in the stiffness analysis have intuitive forms of expression and clear physical meanings. Based on this stiffness model, the stiffness index based on the virtual work, which is proposed by Yan et al. [34], is used to evaluate the capability of the redundantly actuated 2UPR–2PRU PM to resist deformation, which is directly related to the magnitude and direction of external loads. The stiffness index used in this paper can unify the units of translation and rotation [34], and the influence of external forces and couples on the deformation can be uniformly expressed in the inverse of joules. The stiffness distributions of the 2UPR–2PRU PM under various external loads and operational heights are obtained and discussed. All the results can be used as references for future work, such as error modeling and trajectory planning.

This paper is expanded as follows. Section 2 briefly introduces the structure and inverse displacement of the 2UPR–2PRU PM with actuation redundancy. Section 3 carries out the elastostatic stiffness model and stiffness performance of the 2UPR–2PRU PM using the strain energy. Section 4 discusses the stiffness performance in detail, including the influence of the type of external loads and operational height, and the relationship between the stiffness index and singular configurations. Section 5 presents the conclusions.

2. Structural Description and Inverse Displacement Analysis of the Redundantly Actuated 2UPR–2PRU PM

2.1. Structural Description

The three-dimensional model and schematic diagram of the redundantly actuated 2UPR–2PRU PM [32] are shown in Figure 1, which mainly includes four parts: i.e., a fixed base with some bearing supports and guides, a moving platform, two identical UPR kinematic limbs (B_1A_1 and B_2A_2), and two identical PRU kinematic limbs (B_3A_3 and B_4A_4). Two coordinate frames, a fixed frame *O-xyz* and a moving frame *o-uvw*, are set to express the joint coordinates clearly, as shown in Figure 1. In the frame *O-xyz*, the origin point O is fixed on the midpoint of B_1B_2. The *x*-axis is along the direction of $B_3'B_4'$, and the *y*-axis is always along the direction of B_1B_2. In the frame *o-uvw*, the origin point o is fixed on the midpoint of A_1A_2. The *u*-axis points along the oA_4, while the *v*-axis points along the oA_2. The points B_3' and B_4' are the intersection points of the moving direction of two sliders and the *xOy* plane, respectively. In addition, the point o' is defined as the endpoint of the tool mounted on the moving platform. In this study, the link parameters are defined as follows:

$oA_1 = oA_2 = l_1$, $OB_1 = OB_2 = l_2$, $oA_3 = oA_4 = l_3$, $OB'_3 = OB'_4 = l_4$, $B_3A_3 = B_4A_4 = l$, and $oo' = h$.
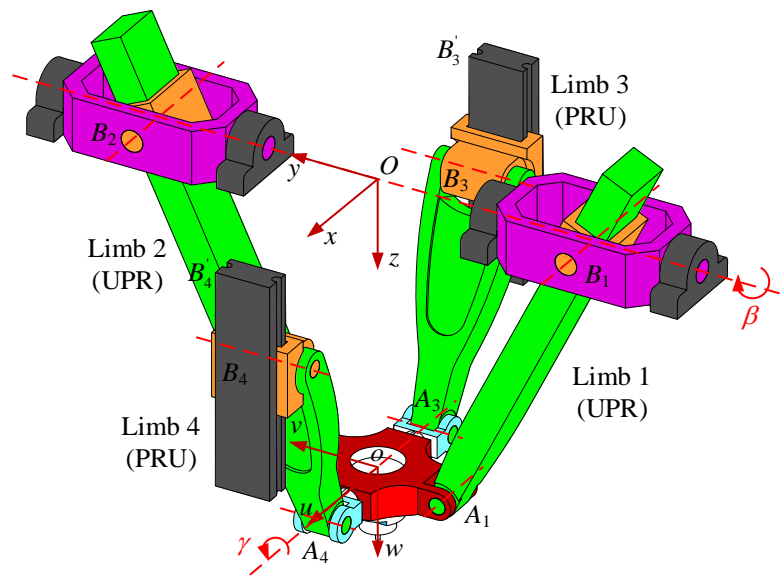
(**a**)
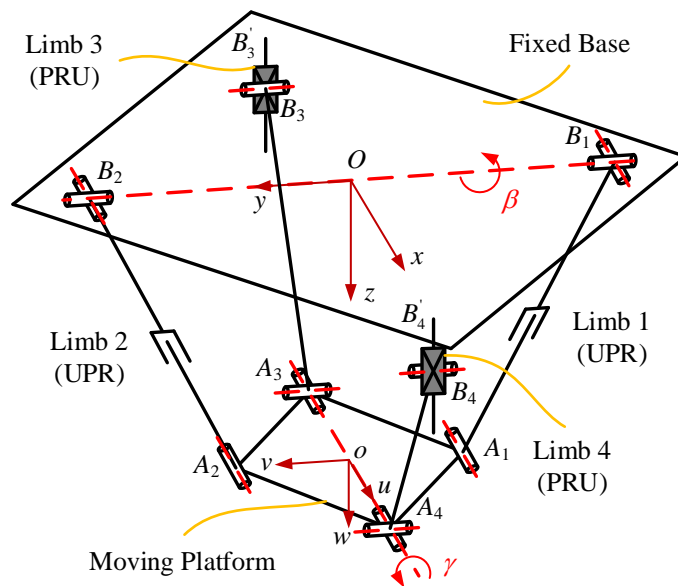
(**b**)

Figure 1. Three-dimensional model of the redundantly actuated 2UPR–2PRU PM: (**a**) three-dimensional model; (**b**) schematic diagram.

For the redundantly actuated 2UPR–2PRU PM, it has been proved that the moving platform can output the continuous motion with three DoFs: i.e., two rotational DoFs (rotation through β and γ) and one translational DoF [32]. The structural constraints of the 2UPR–2PRU PM are briefly introduced below. In the two UPR kinematic limbs, the first rotational axes of the U joints are colinear, and the second rotational axes of the U joints are always parallel to the rotational axes of the R joints connected to the moving platform. In the two PRU kinematic limbs, the first rotational axes of the U joints are parallel to the rotational axes of the R joints connected to the sliders. The second rotational axes of the U joints are colinear.

2.2. Inverse Displacement Analysis

Based on the above structural description, the inverse displacement analysis of the redundantly actuated 2UPR–2PRU PM can be deduced, which is done to develop the relationship between the displacement distances q_i (i = 1, 2, 3, and 4) in the limbs and the orientation and position parameters (β, γ, and z_o), where z_o means the distance of point o along the z-axis. Readers are referred to [32] for the details of the inverse kinematics procedure, and a simple derivation is reviewed here for the following elastostatic stiffness modeling and performance evaluation only.

The rotation matrix that describes the orientation variations of the moving platform with respect to the frame *O-xyz* can be written as

$$
{}^{O}\boldsymbol{R}_o = \begin{pmatrix} c_\beta & s_\beta s_\gamma & s_\beta c_\gamma \\ 0 & c_\gamma & -s_\gamma \\ -s_\beta & c_\beta s_\gamma & c_\beta c_\gamma \end{pmatrix} \tag{1}
$$

where s and c denote the sine and cosine functions, respectively.

Based on the structural constraints in Figure 1, the position vectors of points A_i (i = 1, 2, 3, and 4) can be deduced as

$$
\boldsymbol{p} + \boldsymbol{a}_i = \boldsymbol{b}_i + \boldsymbol{c}_i \tag{2}
$$

where $\boldsymbol{p} = \begin{pmatrix} z_o \tan_\beta & 0 & z_o \end{pmatrix}^{\mathrm{T}}$ is the position vector of point o relative to the *O-xyz*, where tan denotes the tangent function. $\boldsymbol{c}_i$ denotes the position vector of $B_i A_i$ (i = 1, 2, 3, and 4). $\boldsymbol{a}_i$ and $\boldsymbol{b}_i$ denote the position vectors of $o A_i$ and $O B_i$, respectively, and can be expressed as

$$
\begin{cases} \boldsymbol{a}_1 = {}^{O}\boldsymbol{R}_o \begin{pmatrix} 0 & -l_1 & 0 \end{pmatrix}^{\mathrm{T}}, \ \boldsymbol{a}_2 = {}^{O}\boldsymbol{R}_o \begin{pmatrix} 0 & l_1 & 0 \end{pmatrix}^{\mathrm{T}}, \ \boldsymbol{a}_3 = {}^{O}\boldsymbol{R}_o \begin{pmatrix} -l_3 & 0 & 0 \end{pmatrix}^{\mathrm{T}}, \ \boldsymbol{a}_4 = {}^{O}\boldsymbol{R}_o \begin{pmatrix} l_3 & 0 & 0 \end{pmatrix}^{\mathrm{T}} \\ \boldsymbol{b}_1 = \begin{pmatrix} 0 & -l_2 & 0 \end{pmatrix}^{\mathrm{T}}, \ \boldsymbol{b}_2 = \begin{pmatrix} 0 & l_2 & 0 \end{pmatrix}^{\mathrm{T}}, \ \boldsymbol{b}_3 = \begin{pmatrix} -l_4 & 0 & q_3 \end{pmatrix}^{\mathrm{T}}, \ \boldsymbol{b}_4 = \begin{pmatrix} l_4 & 0 & q_4 \end{pmatrix}^{\mathrm{T}} \end{cases} \tag{3}
$$

Substituting the above results into Equation (2), the expressions of q_i (i = 1, 2, 3, and 4) can be written as

$$
\begin{cases} q_1 = \sqrt{\left(z_o \sec_\beta - l_1 s_\gamma\right)^2 + \left(l_2 - l_1 c_\gamma\right)^2} \\ q_2 = \sqrt{\left(z_o \sec_\beta + l_1 s_\gamma\right)^2 + \left(l_1 c_\gamma - l_2\right)^2} \\ q_3 = z_o + l_3 s_\beta - \sqrt{l^2 - \left(z_o \tan_\beta + l_4 - l_3 c_\beta\right)^2} \\ q_4 = z_o - l_3 s_\beta - \sqrt{l^2 - \left(z_o \tan_\beta - l_4 + l_3 c_\beta\right)^2} \end{cases} \tag{4}
$$

A motion simulation is presented here to verify the correctness of the inverse displacement solutions. The link parameters of the redundantly actuated 2UPR–2PRU PM in this simulation are set as follows: l_1 = 27 mm, l_2 = 80 mm, l_3 = 34 mm, l_4 = 70 mm, l = 85 mm, and h = 30 mm. To show the three output DOFs of 2UPR–2PRU PM clearly, a helical motion trajectory is selected as the verification trajectory, and it can be written as follows:

$$
x_{tool} = r c(\omega t) = 5 c(\pi t/2), \ y_{tool} = r s(\omega t) = 5 s(\pi t/2), \ z_{tool} = z_{o'} + h\omega t = 120 + 2\pi t/2 \tag{5}
$$

where r, ω, and h are the radius, angular velocity, and pitch of the helical trajectory, respectively. $z_{o'}$ denotes the initial z-axis component of the endpoint of the tool, and x_{tool}, y_{tool}, and z_{tool} denote the components of the endpoint of the tool on the x-, y-, and z-axes, respectively. The simulation time t is set as 20 s here.

Through the process of inverse kinematics derived above, the actuated displacements of four limbs can be calculated, and the results with respect to the simulation time are shown in Figure 2a. Moreover, by importing these data into the Solidworks software, the simulation trajectory can be obtained. The comparison between the simulation and theoretical trajectories can be easily obtained, as shown in Figure 2b,c, which are mainly about the coincidence of the trajectory points. It is obvious that all the distance errors between

the simulation and theoretical trajectory points, Δ_{output}, are less than 1.2×10^{-6} mm, which could be due to calculation errors. The above results demonstrate the correctness of the inverse displacement.

(a)

(b)

(c)
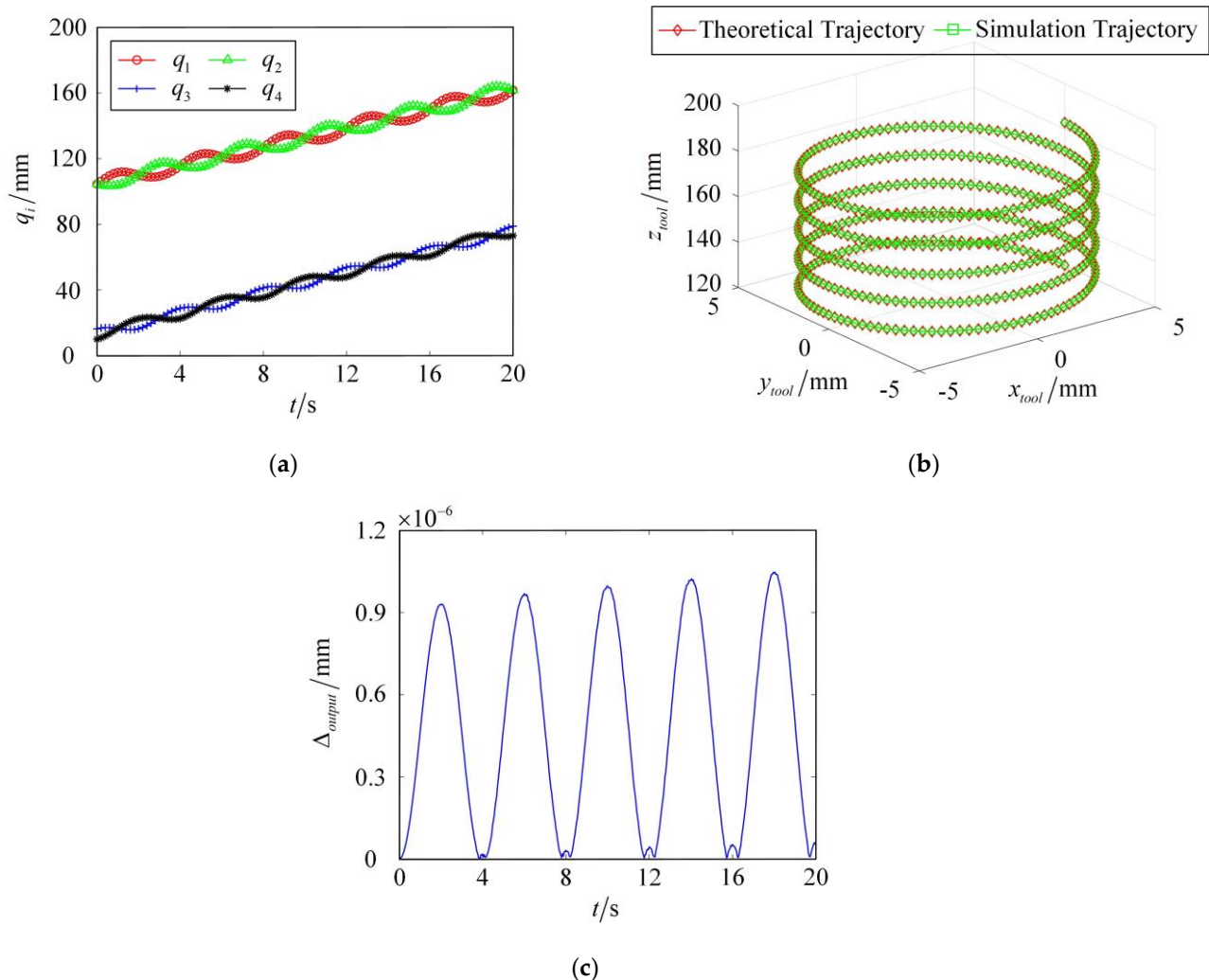
Figure 2. Comparisons of simulation and theoretical results in a given helical trajectory: (**a**) actuated displacements of q_i; (**b**) simulation and theoretical trajectories; (**c**) distance errors between the simulation and theoretical trajectories.

3. Elastostatic Stiffness Modeling of the Redundantly Actuated 2UPR–2PRU PM

The modeling procedure of the elastostatic stiffness of the redundantly actuated 2UPR–2PRU PM is presented in this section, which is mainly based on the screw theory and strain energy [33,34]. The elastostatic stiffness model of the PM involves the limb stiffness model and the overall stiffness model. The results obtained from the stiffness model can be used to evaluate the impact of external loads on the PM, which is necessary for the design stage. Before developing the stiffness model of the redundantly actuated 2UPR–2PRU PM, some simple assumptions should be made. First, the structures of the joints, fixed base, and moving platform are defined as rigid, and only the compliance of the kinematic limbs is considered in this study. Second, the weights of all the components in the system are negligible [35–38], and the influence of friction is omitted.

3.1. Stiffness Matrices of UPR Limbs

In this section, the wrenches including actuation and constraint are determined first. Based on the results in [32] and the limb structure in Figure 1 Reference source not found,

one actuation wrench, $\$_1^T$, and two constraint wrenches, $\$_{11}^r$ and $\$_{12}^r$, of the first UPR limb can be deduced, where $\$_1^T$ represents the actuation force passing through the point B_1 and along the B_1A_1, $\$_{11}^r$ represents the constraint force passing through the point B_1 and along the rotational axis of the R joint, and $\$_{12}^r$ represents the constraint couple perpendicular to the U joint. The magnitudes of these wrenches are defined as f_{11}, f_{12}, and m_{11}, respectively, as shown in Figure 3a.
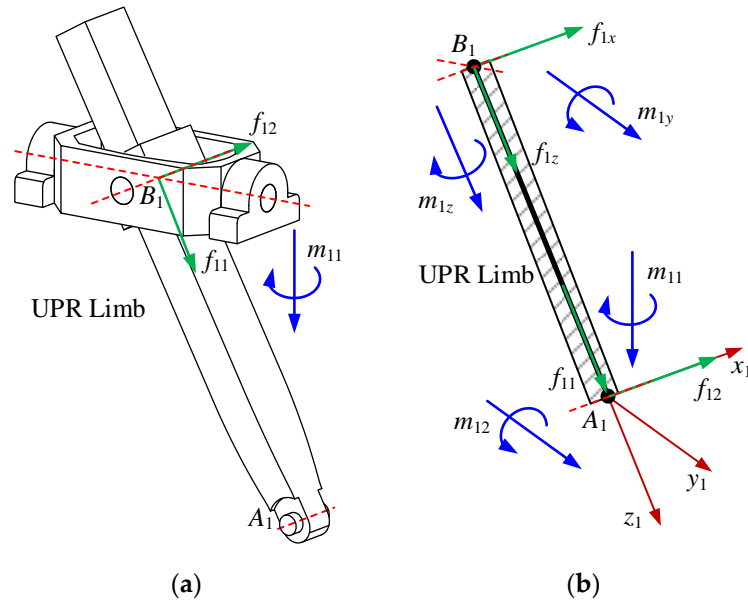
Figure 3. Distributions of wrenches exerted on the UPR limbs: (**a**) wrenches in the UPR limb; (**b**) projections of the wrenches in the UPR limb.

A limb coordinate frame $A_1 - x_1y_1z_1$ is established for the convenience of projecting these wrenches, as shown in Figure 3b, where the x_1-axis points along the axis of the R joint, and the z_1-axis points along B_1A_1. Furthermore, the force f_{12} acting at B_1 can be equivalent to a force f_{12} acting at the point A_1 and a couple $\boldsymbol{m}_{12}$ along the y_1-axis, and the $\boldsymbol{m}_{12}$ can be expressed as

$$\boldsymbol{m}_{12} = -q_1\boldsymbol{z}_1 \times f_{12}\boldsymbol{x}_1 = -q_1 f_{12}\boldsymbol{y}_1 = m_{12}\boldsymbol{y}_1 \tag{6}$$

As shown in Figure 3b, the internal forces/torques at any cross-section of the first UPR kinematic limb can be written as

$$\begin{cases} f_{1x} = f_{12}\boldsymbol{x}_1 \cdot \boldsymbol{x}_1 = f_{12} \\ f_{1y} = 0 \\ f_{1z} = f_{11}\boldsymbol{z}_1 \cdot \boldsymbol{z}_1 = f_{11} \\ m_{1x} = 0 \\ m_{1y} = (v_1\boldsymbol{z}_1 \times f_{12}\boldsymbol{x}_1) \cdot \boldsymbol{y}_1 + m_{11}\boldsymbol{n}_1 \cdot \boldsymbol{y}_1 + m_{12}\boldsymbol{y}_1 \cdot \boldsymbol{y}_1 = m_{11}\boldsymbol{n}_1 \cdot \boldsymbol{y}_1 - q_1 f_{12} + v_1 f_{12} \\ m_{1z} = m_{11}\boldsymbol{n}_1 \cdot \boldsymbol{z}_1 + m_{12}\boldsymbol{y}_1 \cdot \boldsymbol{z}_1 = m_{11}\boldsymbol{n}_1 \cdot \boldsymbol{z}_1 \end{cases} \tag{7}$$

where $\boldsymbol{n}_1$ denotes the direction of the couple $\boldsymbol{m}_{11}$, and v_1 denotes the distance from the cross-section to the point A_1.

The strain energy of the first UPR limb can thus be expressed as

$$\begin{aligned} U_1 &= \int_0^{q_1}\left(\frac{f_{1x}^2}{2G_{q_1}A_{q_1x}} + \frac{f_{1z}^2}{2E_{q_1}A_{q_1}} + \frac{m_{1y}^2}{2E_{q_1}I_{q_1y}} + \frac{m_{1z}^2}{2G_{q_1}J_{q_1}} \right)dv_1 \\ &= \frac{q_1}{2G_{q_1}A_{q_1x}}f_{12}^2 + \frac{q_1}{2E_{q_1}A_{q_1}}f_{11}^2 + \int_0^{q_1}\left(\frac{(m_{11}\boldsymbol{n}_1\cdot\boldsymbol{y}_1 - q_1f_{12} + v_1f_{12})^2}{2E_{q_1}I_{q_1y}} \right)dv_1 + \frac{(\boldsymbol{n}_1\cdot\boldsymbol{z}_1)^2 q_1}{2G_{q_1}J_{q_1}}m_{11}^2 \\ &= \frac{q_1}{2G_{q_1}A_{q_1x}}f_{12}^2 + \frac{q_1}{2E_{q_1}A_{q_1}}f_{11}^2 + \frac{q_1^3}{6E_{q_1}I_{q_1y}}f_{12}^2 - \frac{\boldsymbol{n}_1\cdot\boldsymbol{y}_1 q_1^2}{2E_{q_1}I_{q_1y}}f_{12}m_{11} + \frac{(\boldsymbol{n}_1\cdot\boldsymbol{y}_1)^2 q_1}{2E_{q_1}I_{q_1y}}m_{11}^2 + \frac{(\boldsymbol{n}_1\cdot\boldsymbol{z}_1)^2 q_1}{2G_{q_1}J_{q_1}}m_{11}^2 \end{aligned} \tag{8}$$

where E_{q_1} and G_{q_1} denote the elastic and shear modulus of limb 1, respectively. A_{q_1} denotes the area of the cross-section of limb 1, and $A_{q_1 x}$ denotes the effective shear area of the cross-section along the x_1-axis. $I_{q_1 y}$ denotes the area moment of inertia of the cross-section about the y_1-axis, and J_{q_1} denotes the polar moment of inertia of the cross-section.

Then, the deformations of this limb along the directions of these three wrenches, $\boldsymbol{\delta}_{L_1} = \begin{pmatrix} \delta_{11} & \delta_{12} & \psi_{11} \end{pmatrix}^{\mathrm{T}}$, can be obtained as

$$
\begin{cases}
\delta_{11} = \dfrac{\partial U_1}{\partial f_{11}} = \dfrac{q_1}{E_{q_1} A_{q_1}} f_{11} \\[2ex]
\delta_{12} = \dfrac{\partial U_1}{\partial f_{12}} = \dfrac{q_1}{G_{q_1} A_{q_1 x}} f_{12} + \dfrac{q_1^3}{3 E_{q_1} I_{q_1 y}} f_{12} - \dfrac{\boldsymbol{n}_1 \cdot \boldsymbol{y}_1 q_1^2}{2 E_{q_1} I_{q_1 y}} m_{11} \\[2ex]
\psi_{11} = \dfrac{\partial U_1}{\partial m_{11}} = -\dfrac{\boldsymbol{n}_1 \cdot \boldsymbol{y}_1 q_1^2}{2 E_{q_1} I_{q_1 y}} f_{12} + \dfrac{(\boldsymbol{n}_1 \cdot \boldsymbol{y}_1)^2 q_1}{E_{q_1} I_{q_1 y}} m_{11} + \dfrac{(\boldsymbol{n}_1 \cdot \boldsymbol{z}_1)^2 q_1}{G_{q_1} J_{q_1}} m_{11}
\end{cases}
\tag{9}
$$

The above results can be written in the matrix form of the relationship between the deformations and wrenches as

$$
\begin{pmatrix} \delta_{11} & \delta_{12} & \psi_{11} \end{pmatrix}^{\mathrm{T}} = \boldsymbol{C}_{L_1} \begin{pmatrix} f_{11} & f_{12} & m_{11} \end{pmatrix}^{\mathrm{T}}
\tag{10}
$$

and

$$
\boldsymbol{C}_{L_1} = \begin{pmatrix}
\dfrac{q_1}{E_{q_1} A_{q_1}} & 0 & 0 \\[2ex]
0 & \dfrac{q_1}{G_{q_1} A_{q_1 x}} + \dfrac{q_1^3}{3 E_{q_1} I_{q_1 y}} & -\dfrac{\boldsymbol{n}_1 \cdot \boldsymbol{y}_1 q_1^2}{2 E_{q_1} I_{q_1 y}} \\[2ex]
0 & -\dfrac{\boldsymbol{n}_1 \cdot \boldsymbol{y}_1 q_1^2}{2 E_{q_1} I_{q_1 y}} & \dfrac{(\boldsymbol{n}_1 \cdot \boldsymbol{y}_1)^2 q_1}{E_{q_1} I_{q_1 y}} + \dfrac{(\boldsymbol{n}_1 \cdot \boldsymbol{z}_1)^2 q_1}{G_{q_1} J_{q_1}}
\end{pmatrix}
\tag{11}
$$

The stiffness matrix $\boldsymbol{K}_{L_1}$ of limb 1 can thus be written as the inverse of the compliance matrix $\boldsymbol{C}_{L_1}$ as

$$
\boldsymbol{K}_{L_1} = \boldsymbol{C}_{L_1}^{-1}
\tag{12}
$$

3.2. Stiffness Matrices of PRU Limbs

The process of calculating the stiffness matrix of the PRU limb is introduced below, which is similar to that of the UPR limb. For the PRU limb, one actuation wrench, $\$_3^{\mathrm{T}}$, and two constraint wrenches, $\$_{31}^r$ and $\$_{32}^r$, also should be determined first. Based on the results in [32], $\$_3^{\mathrm{T}}$ represents the actuation force passing through the point B_3 and along the $B_3 A_3$, $\$_{31}^r$ represents the constraint force passing through the point A_3 and along the rotational axis of the R joint, and $\$_{32}^r$ represents the constraint couple perpendicular to the U joint. The magnitudes of these wrenches are defined as f_{31}, f_{32}, and m_{31}, respectively, as shown in Figure 4a.
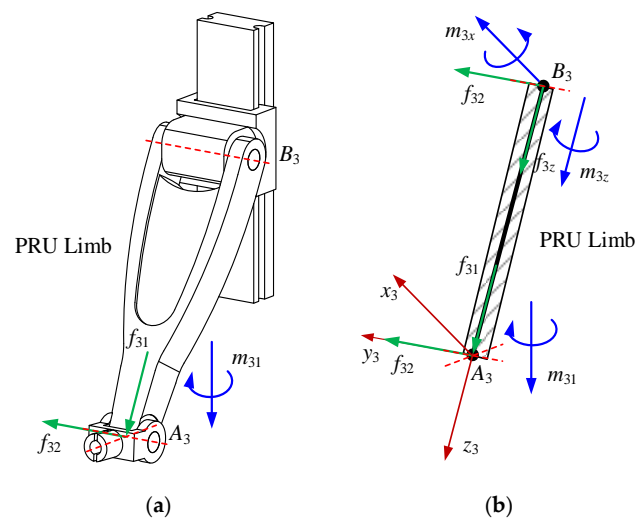
Figure 4. Distributions of wrenches exerted on the PRU limbs: (**a**) wrenches in the PRU limb; (**b**) projections of the wrenches in the PRU limb.

The decomposed results of three wrenches along the axes of the limb coordinate frame $A_3 - x_3 y_3 z_3$ are shown in Figure 4b, in which the directions of y_3 and z_3-axes are along the rotational axis of the R joint and $B_3 A_3$, respectively. The internal projection forces/torques at any cross-section of the PRU limb along the directions of local axes can be written as

$$
\begin{cases}
f_{3x} = 0 \\
f_{3y} = f_{32} \boldsymbol{y}_3 \cdot \boldsymbol{y}_3 = f_{32} \\
f_{3z} = f_{31} \boldsymbol{z}_3 \cdot \boldsymbol{z}_3 = f_{31} \\
m_{3x} = (v_3 \boldsymbol{z}_3 \times f_{32} \boldsymbol{y}_3) \cdot \boldsymbol{x}_3 + m_{31} \boldsymbol{n}_3 \cdot \boldsymbol{x}_3 = m_{31} \boldsymbol{n}_3 \cdot \boldsymbol{x}_3 - v_3 f_{32} \\
m_{3y} = 0 \\
m_{3z} = m_{31} \boldsymbol{n}_3 \cdot \boldsymbol{z}_3
\end{cases}
\tag{13}
$$

where $\boldsymbol{n}_3$ denotes the direction of the couple m_{31}, and v_3 denotes the distance between the cross-section and A_3.

The strain energy of the first PRU limb can thus be expressed as

$$
\begin{aligned}
U_3 &= \int_0^l \left(\frac{f_{3y}^2}{2G_l A_{ly}} + \frac{f_{3z}^2}{2E_l A_l} + \frac{m_{3x}^2}{2E_l I_{lx}} + \frac{m_{3z}^2}{2G_l J_l} \right) dv_3 \\
&= \frac{l}{2G_l A_{ly}} f_{32}^2 + \frac{l}{2E_l A_l} f_{31}^2 + \int_0^l \left(\frac{(m_{31} \boldsymbol{n}_3 \cdot \boldsymbol{x}_3 - v_3 f_{32})^2}{2E_l I_{lx}} \right) dv_3 + \frac{(\boldsymbol{n}_3 \cdot \boldsymbol{z}_3)^2 l}{2G_l J_l} m_{31}^2 \\
&= \frac{l}{2G_l A_{ly}} f_{32}^2 + \frac{l}{2E_l A_l} f_{31}^2 + \frac{l^3}{6E_l I_{lx}} f_{32}^2 - \frac{\boldsymbol{n}_3 \cdot \boldsymbol{x}_3 l^2}{2E_l I_{lx}} f_{32} m_{31} + \frac{(\boldsymbol{n}_3 \cdot \boldsymbol{x}_3)^2 l}{2E_l I_{lx}} m_{31}^2 + \frac{(\boldsymbol{n}_3 \cdot \boldsymbol{z}_3)^2 l}{2G_l J_l} m_{31}^2
\end{aligned}
\tag{14}
$$

where E_l and G_l denote the elastic and shear modulus of limb 3, respectively. A_l denotes the area of the cross-section of limb 3, and A_{ly} denotes the effective shear area of the cross-section along the y_3-axis. I_{lx} denotes the area moment of inertia of the cross-section about the x_3-axis, and J_l denotes the polar moment of inertia of the cross-section.

Similarly, the relationship between the deformations of the first PRU limb, $\boldsymbol{\delta}_{L_3} = \begin{pmatrix} \delta_{31} & \delta_{32} & \psi_{31} \end{pmatrix}^{\mathrm{T}}$, and wrenches also can be written as

$$
\begin{pmatrix} \delta_{31} & \delta_{32} & \psi_{31} \end{pmatrix}^{\mathrm{T}} = \boldsymbol{C}_{L_3} \begin{pmatrix} f_{31} & f_{32} & m_{31} \end{pmatrix}^{\mathrm{T}}
\tag{15}
$$

and

$$
\boldsymbol{C}_{L_3} = \begin{pmatrix}
\frac{l}{E_l A_l} & 0 & 0 \\
0 & \frac{l}{G_l A_{ly}} + \frac{l^3}{3E_l I_{lx}} & -\frac{\boldsymbol{n}_3 \cdot \boldsymbol{x}_3 l^2}{2E_l I_{lx}} \\
0 & -\frac{\boldsymbol{n}_3 \cdot \boldsymbol{x}_3 l^2}{2E_l I_{lx}} & \frac{(\boldsymbol{n}_3 \cdot \boldsymbol{x}_3)^2 l}{E_l I_{lx}} + \frac{(\boldsymbol{n}_3 \cdot \boldsymbol{z}_3)^2 l}{G_l J_l}
\end{pmatrix}
\tag{16}
$$

The stiffness matrix $\boldsymbol{K}_{L_3}$ of limb 3 can thus be written as

$$
\boldsymbol{K}_{L_3} = \boldsymbol{C}_{L_3}^{-1}
\tag{17}
$$

Through the above analysis, the strain energy of limbs can be obtained, followed by the stiffness matrices of the UPR limb and PRU limb. It should be noted that each link in the above study is assumed with a uniform cross-section, as explained in Equations (8) and (14). For other links with complicated structures, such as step links with different cross-sections and links with gradient cross-sections, the expressions of Equations (8) and (14) should be modified accordingly. At this time, the area, effective shear area, area moment of the inertia, and polar moment of inertia of the cross-section will not be constant, which will be the focus of our follow-up research.

3.3. Overall Stiffness Matrix of the 2UPR–2PRU PM

For the 2UPR–2PRU PM, the small configuration variations of the point in the moving platform can reflect the overall stiffness performance, which is determined by the reaction wrenches from the four limbs and external load $\boldsymbol{W}_M$, as shown in Figure 5. The external load $\boldsymbol{W}_M = \begin{pmatrix} \boldsymbol{F}^{\mathrm{T}} & \boldsymbol{M}^{\mathrm{T}} \end{pmatrix}^{\mathrm{T}}$ acts on the origin of the moving platform, in which $\boldsymbol{F}$ and $\boldsymbol{M}$ denote the

vectors of applied external force and moment, respectively. First, the equilibrium equations that describe the reaction wrenches and external loads can be directly obtained as

$$W_M = \begin{pmatrix} W_{L_1} & W_{L_2} & W_{L_3} & W_{L_4} \end{pmatrix} \begin{pmatrix} f_{L_1} & f_{L_2} & f_{L_3} & f_{L_4} \end{pmatrix} = W_L f_L \tag{18}$$

where $W_{L_1} = \begin{pmatrix} \$_1^T & \$_{11}^r & \$_{12}^r \end{pmatrix}$, $W_{L_2} = \begin{pmatrix} \$_2^T & \$_{21}^r & \$_{22}^r \end{pmatrix}$, $W_{L_3} = \begin{pmatrix} \$_3^T & \$_{31}^r & \$_{32}^r \end{pmatrix}$, and $W_{L_4} = \begin{pmatrix} \$_4^T & \$_{41}^r & \$_{42}^r \end{pmatrix}$ denote the wrench matrices of four limbs, respectively. $f_{L_1} = \begin{pmatrix} f_{11} & f_{12} & m_{11} \end{pmatrix}^T$, $f_{L_2} = \begin{pmatrix} f_{21} & f_{22} & m_{21} \end{pmatrix}^T$, $f_{L_3} = \begin{pmatrix} f_{31} & f_{32} & m_{31} \end{pmatrix}^T$, and $f_{L_4} = \begin{pmatrix} f_{41} & f_{42} & m_{41} \end{pmatrix}^T$ denote the magnitude vectors of four limbs, respectively.
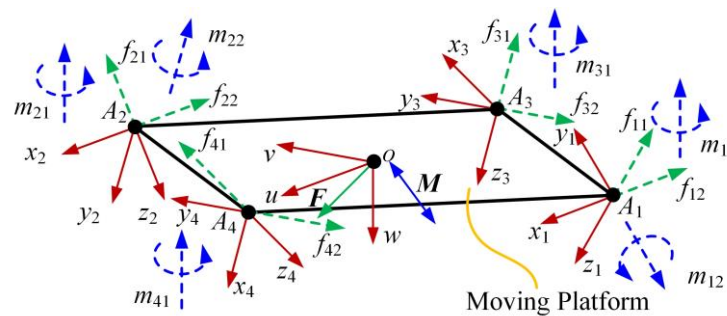
Figure 5. Reaction forces and external loads acting on the moving platform.

Then, the deformation of the origin of the moving platform $D_M = \begin{pmatrix} \delta x & \delta y & \delta z & \delta\theta & \delta\varphi & \delta\psi \end{pmatrix}^T$ can be related to the deformations along the direction of wrenches in all limbs as

$$W_M^T D_M = f_{L_1}^T \delta_{L_1} + f_{L_2}^T \delta_{L_2} + f_{L_3}^T \delta_{L_3} + f_{L_4}^T \delta_{L_4} \tag{19}$$

from which the relationship between δ_{L_i} (i = 1, 2, 3, and 4) and D_M can be expressed as $\delta_{L_i} = W_{L_i}^T D_M$.

Based on the above results, the mapping between the external loads and deformation vector can be obtained as

$$W_M = W_{L_1} K_{L_1} W_{L_1}^T D_M + W_{L_2} K_{L_2} W_{L_2}^T D_M + W_{L_3} K_{L_3} W_{L_3}^T D_M + W_{L_4} K_{L_4} W_{L_4}^T D_M = \sum_{i=1}^{4} W_{L_i} K_{L_i} W_{L_i}^T D_M = K_M D_M \tag{20}$$

from which the stiffness matrix K_M of the 2UPR–2PRU redundantly actuated PM can be written as

$$K_M = \sum_{i=1}^{4} W_{L_i} K_{L_i} W_{L_i}^T \tag{21}$$

In summary, the analytical limb and overall stiffness models of the redundantly actuated 2UPR–2PRU PM have been developed, which have intuitive forms of expression and clear physical meanings. These theoretical results also can provide references for actual applications, such as the trajectory planning of prototypes.

3.4. Comparisons of Theoretical Results with the FEA Method

In this section, the FEA method is used to verify the correctness of the theoretical stiffness model of the 2UPR–2PRU PM with actuation redundancy. Under the external load, the precise stiffness and deformation results of the PM can be provided by establishing the corresponding finite element model in ANSYS software. In the finite element model, the connections between the fixed base and the actuated joints are grounded, and the moving platform and all kinematic joints are set as rigid. To obtain the simulation results with high precision, the flexible links in the model are established by using the element beam188 based on the Timoshenko beam theory, which is a three-dimensional beam element with two nodes. Additionally, the beam element is set as quadratic. It considers the shear defor-

mation effects during the simulation and can accurately express the spatial deformations of links. The link parameters, including the lengths and material characteristics of the redundantly actuated 2UPR–2PRU PM, are listed in Table 1. In this paper, the cross-sections of four limbs are defined as the solid circular sections with the same size, $A_{B_i A_i} = A$ (i = 1, 2, 3, and 4), and the elastic modulus and shear modulus of four limbs are the same in this investigation, namely, $E_{B_i A_i} = E$ and $G_{B_i A_i} = G$ (i = 1, 2, 3, and 4). In addition, the Poisson's ratio μ is the same.

Table 1. Length and material parameters of the redundantly actuated 2UPR–2PRU PM.

Parameters	Units	Values
l_1	mm	250
l_2	mm	400
l_3	mm	200
l_4	mm	320
l	mm	670
d	mm	50
A	mm^2	1963.50
G	GPa	80
E	GPa	210
μ	/	0.33
β	rad	$\pm 2\pi/9$
γ	rad	$\pm 2\pi/9$

To demonstrate the correctness of theoretical results, four configurations of redundantly actuated 2UPR–2PRU PM with different external loads are chosen as verified cases in this study, as shown in Table 2. The boundary conditions of the redundantly actuated 2UPR–2PRU PM exported by the ANSYS software are provided in Figure 6, in which the PM in case 1 is taken as an example. The applied constraint situations and external load of the 2UPR–2PRU PM can be found, in which the U joint in the UPR limb is subjected to three translation constraints and one rotation constraint, and the R joint in the RPU limb is subjected to three translation constraints and two rotation constraints. Additionally, an external load is applied to the center point of the moving platform. Figure 7a–h depicts the linear and angular deformations in the four cases in the software ANSYS, which can show the influence of different external loads on the 2UPR–2PRU PM to some extent. In Figure 7a,b, the two rotating angles of the moving platform are zero, and it is only subjected to a simple external load along the z-axis. Since the 2UPR–2PRU PM has a symmetrical structure in this case, the center of the moving platform only has a small linear deformation along the z-axis, and there is no angular deformation. In cases 2 and 3, as shown in Figure 7c–f, since the moving platform is subjected to a combined external load, the moving platform has small linear and angular deformations. The results in the above figures show that the deformation is related to the configuration and external load. In case 4, as shown in Figure 7g,h, the moving platform is subjected to a huge external load, which leads to large linear and angular deformations. Table 3 also lists the values of deformations of the center of the moving platform in four examples by using theoretical and FEA models. In the first three cases with small deformations, the results obtained from the theoretical and FEA models are almost the same, and all the relative errors of deformations in these cases are less than 0.67%, which is very low and can be acceptable. In the fourth case with large deformation, the maximum value of relative errors is only 3.52%, which proves that the theoretical model can also be used for the prediction of the case with large deformation. All the results show that the beam element used in the simulation is enough to validate the theoretical method. The developed theoretical model is universal, which makes it suitable not only for cases with small deformations but also for large deformation prediction. Therefore, the compliance/stiffness matrix of the 2UPR–2PRU PM with actuation redundancy obtained from the theoretical model can be regarded as an alternative to that

obtained from the FEA model and also provide the foundation for the following stiffness performance evaluation.

Table 2. Four selected cases of the redundantly actuated 2UPR–2PRU PM.

Parameters	Units	Case 1	Case 2	Case 3	Case 4
z_o	mm	600	600	600	600
β	rad	0	0	pi/6	pi/6
γ	rad	0	0	pi/6	pi/6
F_x	N	0	100	100	60,000
F_y	N	0	100	100	60,000
F_z	N	100	100	100	100,000
M_x	Nm	0	100	100	60,000
M_y	Nm	0	100	100	60,000
M_z	Nm	0	100	100	100,000
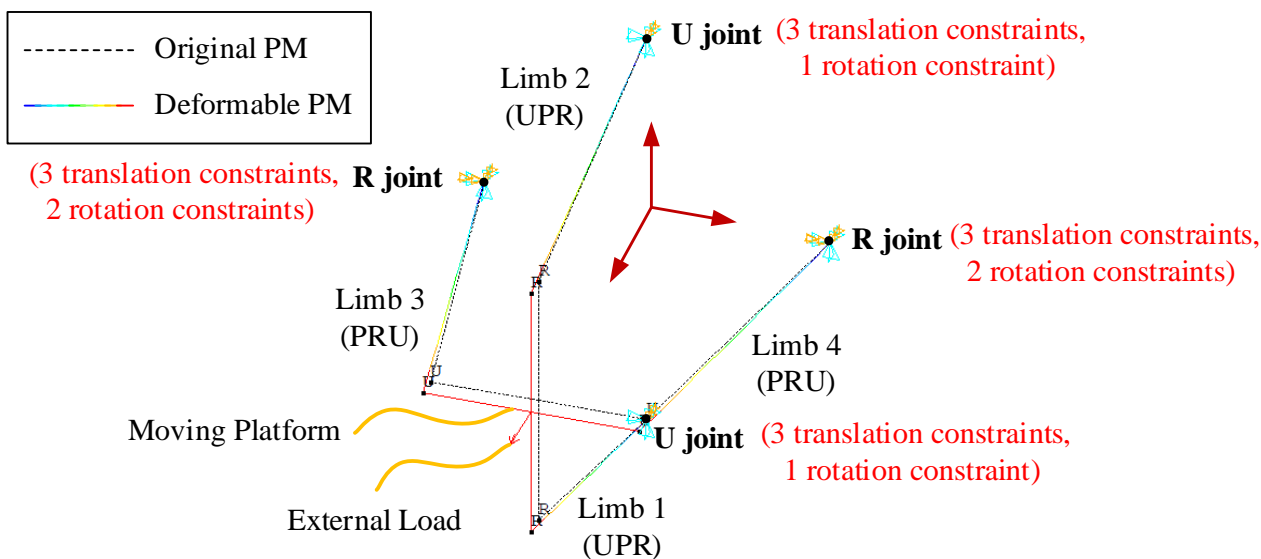
Figure 6. Boundary conditions of the redundantly actuated 2UPR–2PRU PM in ANSYS software.

(**a**)

(**b**)
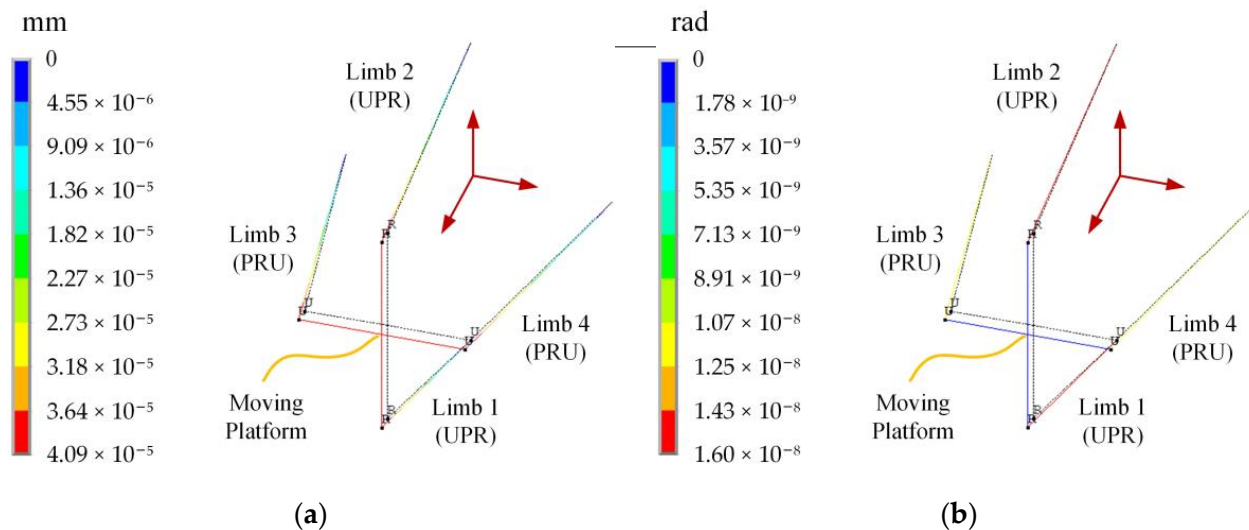
Figure 7. *Cont.*
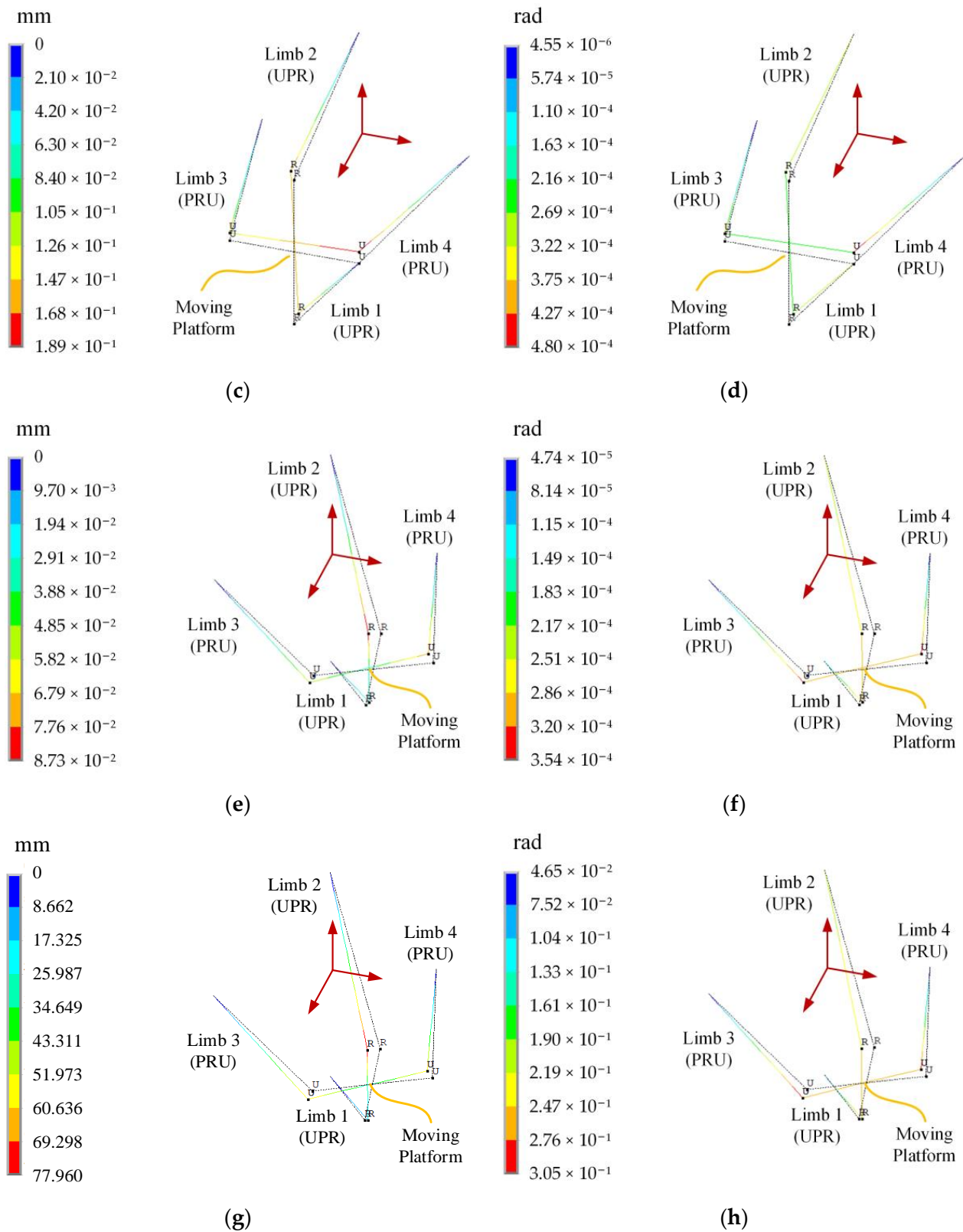
Figure 7. Linear and angular deformations of the redundantly actuated 2UPR–2PRU PM in four selected cases: (**a**) linear deformation of case 1; (**b**) angular deformation of case 1; (**c**) linear deformation of case 2; (**d**) angular deformation of case 2; (**e**) linear deformation of case 3; (**f**) angular deformation of case 3; (**g**) linear deformation of case 4; (**h**) angular deformation of case 4.

Table 3. Comparison results between the FEA method and theoretical method for the deformation in the four selected cases.

Case	Method	Δx (mm)	Δy (mm)	Δz (mm)	$\Delta\theta$ (rad)	$\Delta\varphi$ (rad)	$\Delta\psi$ (rad)
1	Theory value	0	0	4.0884×10^{-5}	0	0	0
	FEA value	-7.1557×10^{-17}	-5.7395×10^{-17}	4.0916×10^{-5}	1.3553×10^{-19}	-1.3553×10^{-19}	1.9588×10^{-20}
	Relative error (%)	/	/	0.08	/	/	/
2	Theory value	3.0794×10^{-3}	1.5333×10^{-1}	4.0884×10^{-5}	1.5461×10^{-4}	-6.2931×10^{-7}	1.7099×10^{-4}
	FEA value	3.0859×10^{-3}	1.5372×10^{-1}	4.0916×10^{-5}	1.5500×10^{-4}	-6.3355×10^{-7}	1.7138×10^{-4}
	Relative error (%)	0.21	0.25	0.08	0.25	0.67	0.23
3	Theory value	-2.6554×10^{-2}	1.1924×10^{-2}	1.5574×10^{-2}	1.5477×10^{-4}	4.3138×10^{-5}	2.3573×10^{-4}
	FEA value	-2.6459×10^{-2}	1.1991×10^{-2}	1.5513×10^{-2}	1.5565×10^{-4}	4.2987×10^{-5}	2.3709×10^{-4}
	Relative error (%)	0.36	0.56	0.39	0.57	0.35	0.57
4	Theory value	-25.9132	-1.4088	15.8888	1.1980×10^{-1}	4.1705×10^{-1}	2.1121×10^{-1}
	FEA value	-25.8250	-1.3609	15.8330	1.2054×10^{-1}	4.1564×10^{-1}	2.1236×10^{-1}
	Relative error (%)	0.34	3.52	0.35	0.61	0.34	0.54

4. Stiffness Performance Evaluation of the Redundantly Actuated 2UPR–2PRU PM

Since the dimensions of elements in the general stiffness matrix are different, some common stiffness indices, such as the maximum and minimum eigenvalues [39] and average of the eigenvalues [11], will lead to unclear physical meanings and erroneous interpretations [40]. In addition, some stiffness indices can separate the translations and rotations [39,41,42], such as the stiffness indices based on the linear stiffness and angular compliance ellipsoids [39]. In this paper, the stiffness index proposed by Yan et al. [34] is used to measure the elastostatic stiffness characteristics of the 2UPR–2PRU PM with actuation redundancy. This criterion evaluates the stiffness property of a PM based on the energy and related to the direction of external load. This index can intuitively measure the capability of the PM to resist the external load in a certain direction, and it is defined as

$$\kappa = 1/W_M^T C_M W_M \tag{22}$$

where C_M is the overall compliance matrix, and $W_M^T C_M W_M = W_M^T D_M$ denotes the virtual work of a PM under the external load. Through the multiplication combination of C_M and W_M, the dimension is unified into the joule (J), and after the inversion, the unit of the index changes into the inverse of the joule (J^{-1}). For example, 1 J^{-1} means that the equivalent deformation of a PM is 1 mm when the external load is 1000 N. It is obvious that the bigger the value of κ, the stiffer the configuration.

Using the link parameters listed in Table 1, the distributions of κ under different single external loads are shown in Figure 8a–f. All of them are limited in operational height $z_o = 600$ mm. Since all of them are symmetric about the plane $\beta = 0°$ and $\gamma = 0°$, only the top-left quarter of each distribution is depicted. The distributions of κ under single external force and couple loads are completely different due to the structural characteristics of the 2UPR–2PRU PM. For the different external force loads, as shown in the results in Figure 8a–c, the orientation ranges of the PM with better stiffness performance are different, and the 2UPR–2PRU PM with actuation redundancy has better resistance to the external force load along the *z*-axis, which is determined by the structure arrangement. For the different external couple loads, as shown in Figure 8d–f, the influence of the couple on the stiffness performance of the 2UPR–2PRU PM is different from that of the force, from which one can find that the 2UPR–2PRU PM has better resistance to the external couple load along the *y*-axis. In addition, the distributions of κ in a combined external load are shown in Figure 8g, which are different from the results in Figure 8a–f. This is caused by the influences of the external load on the overall stiffness of this PM.

(**a**)

(**b**)

(**c**)

(**d**)

(**e**)

(**f**)

Figure 8. *Cont*.

(g)
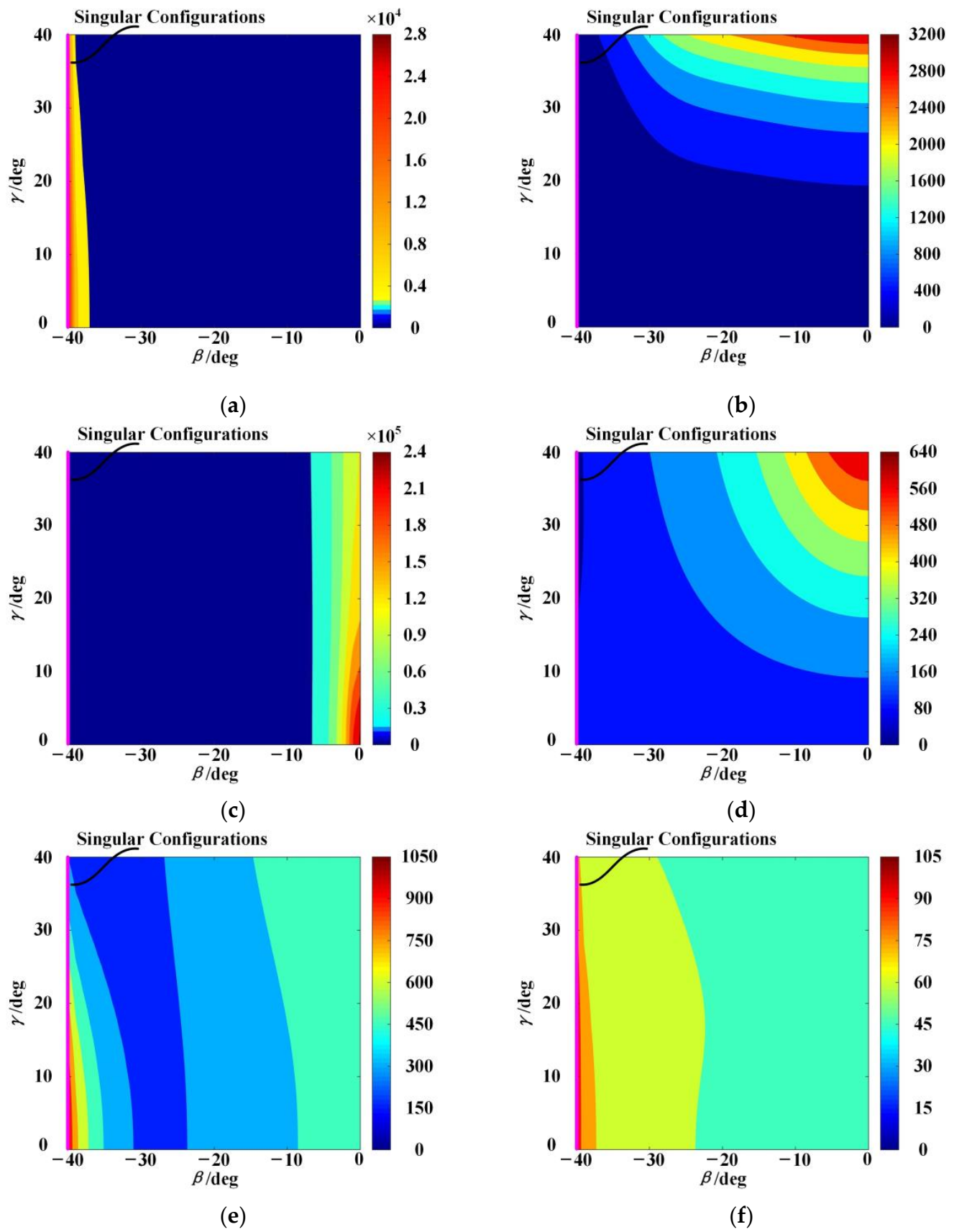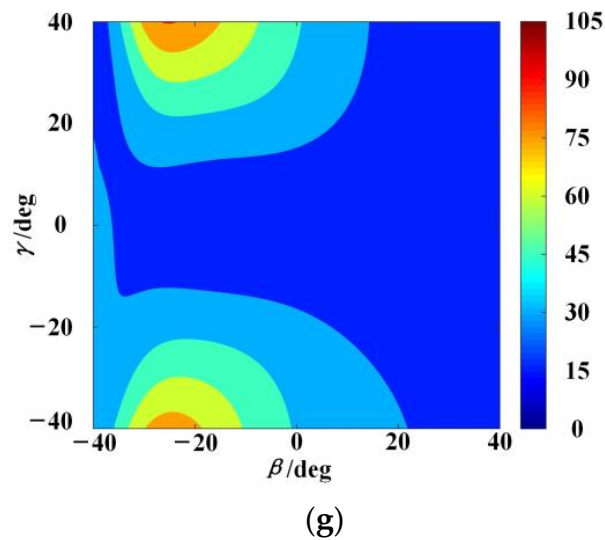
Figure 8. Distributions of κ in the cases with different external loads: **(a)** $W_M = \begin{bmatrix} 100\,\text{N} & 0 & 0 & 0 & 0 & 0 \end{bmatrix}$; **(b)** $W_M = \begin{bmatrix} 0 & 100\,\text{N} & 0 & 0 & 0 & 0 \end{bmatrix}$; **(c)** $W_M = \begin{bmatrix} 0 & 0 & 100\,\text{N} & 0 & 0 & 0 \end{bmatrix}$; **(d)** $W_M = \begin{bmatrix} 0 & 0 & 0 & 100\,\text{Nm} & 0 & 0 \end{bmatrix}$; **(e)** $W_M = \begin{bmatrix} 0 & 0 & 0 & 0 & 100\,\text{Nm} & 0 \end{bmatrix}$; **(f)** $W_M = \begin{bmatrix} 0 & 0 & 0 & 0 & 0 & 100\,\text{Nm} \end{bmatrix}$; **(g)** $W_M = \begin{bmatrix} 100\,\text{N} & 100\,\text{N} & 100\,\text{N} & 100\,\text{Nm} & 100\,\text{Nm} & 100\,\text{Nm} \end{bmatrix}$.

The elastostatic stiffness performance above can also be related to the singularity of the PM. The stiffness performance of the PM in the singular configuration can be clearly described by using the above stiffness indices under single external loads. In [32], it has been proved that the redundantly actuated 2UPR–2PRU PM is in the inverse kinematic singular configurations when the link B_3A_3 or B_4A_4 is parallel to the x-axis. Using the link parameters and operational height above, the 2UPR–2PRU PM reaches the singular configurations when $\beta = -40°$ or $\beta = 40°$, which have been highlighted in pink in the top-left quarter of each distribution, as shown in Figure 8a–f. In Figure 8a–c, the 2UPR–2PRU PM under the singular configurations has better stiffness performance when the single external force is along the x-axis. However, the stiffness performance of the PM is poor when the single external force is along the y- or z-axis. In addition, the 2UPR–2PRU PM under the singular configurations has poor stiffness performance when a single external couple is applied on the moving platform, no matter in what direction, as shown in Figure 8d–f. To summarize, the 2UPR–2PRU PM with redundancy actuation has relatively good resistance to a single external force along the x-axis in singular configurations. Compared with the values of the stiffness index under the external force along the x-axis, these values under other external forces or couples are so small and can be approximated as zero. It should be noted that although the stiffness model developed in this study is a simple one with some assumptions, the above results can provide references for avoiding singular configurations and selecting the suitable workspace.

The distributions of κ under a combined external load in the different operational heights are also discussed in this paper. Figure 9a–d shows the distributions of κ in the different operational heights when $W_M = \begin{bmatrix} 100\,\text{N} & 100\,\text{N} & 100\,\text{N} & 100\,\text{Nm} & 100\,\text{Nm} & 100\,\text{Nm} \end{bmatrix}$. The stiffness performance becomes worse with the increase of the operational height. Under this external load, the redundantly actuated 2UPR–2PRU PM has a better stiffness performance in the orientation ranges where $\beta \in \begin{bmatrix} -40°, & 0° \end{bmatrix}$ and $\gamma \in \begin{bmatrix} -40°, & -20° \end{bmatrix}$, and $\beta \in \begin{bmatrix} -40°, & 0° \end{bmatrix}$ and $\gamma \in \begin{bmatrix} 20°, & 40° \end{bmatrix}$. To demonstrate the superiority of the mechanism stiffness in the selected orientation ranges, the minimum, maximum, and average values of the stiffness index in the above selected ranges and other ranges are listed, as shown in Table 4. It can be seen that in the different operational heights, the minimum, maximum,

and average values of the stiffness index in the above selected orientation ranges are larger than those in the other orientation ranges. The relative proportion ranges from 106.36% to 257.84%. From the results in Figures 8 and 9, it can be concluded that the magnitude and direction of the external load have a major impact on the distributions of stiffness performance of the 2UPR–2PRU PM, which provides guidance for the selection of application scenarios and a suitable workspace. Furthermore, in some special application scenarios where an external load in a specific direction is required, the distributions of stiffness performance can also be used for structural design and trajectory planning [34].

(a)

(b)

(c)

(d)
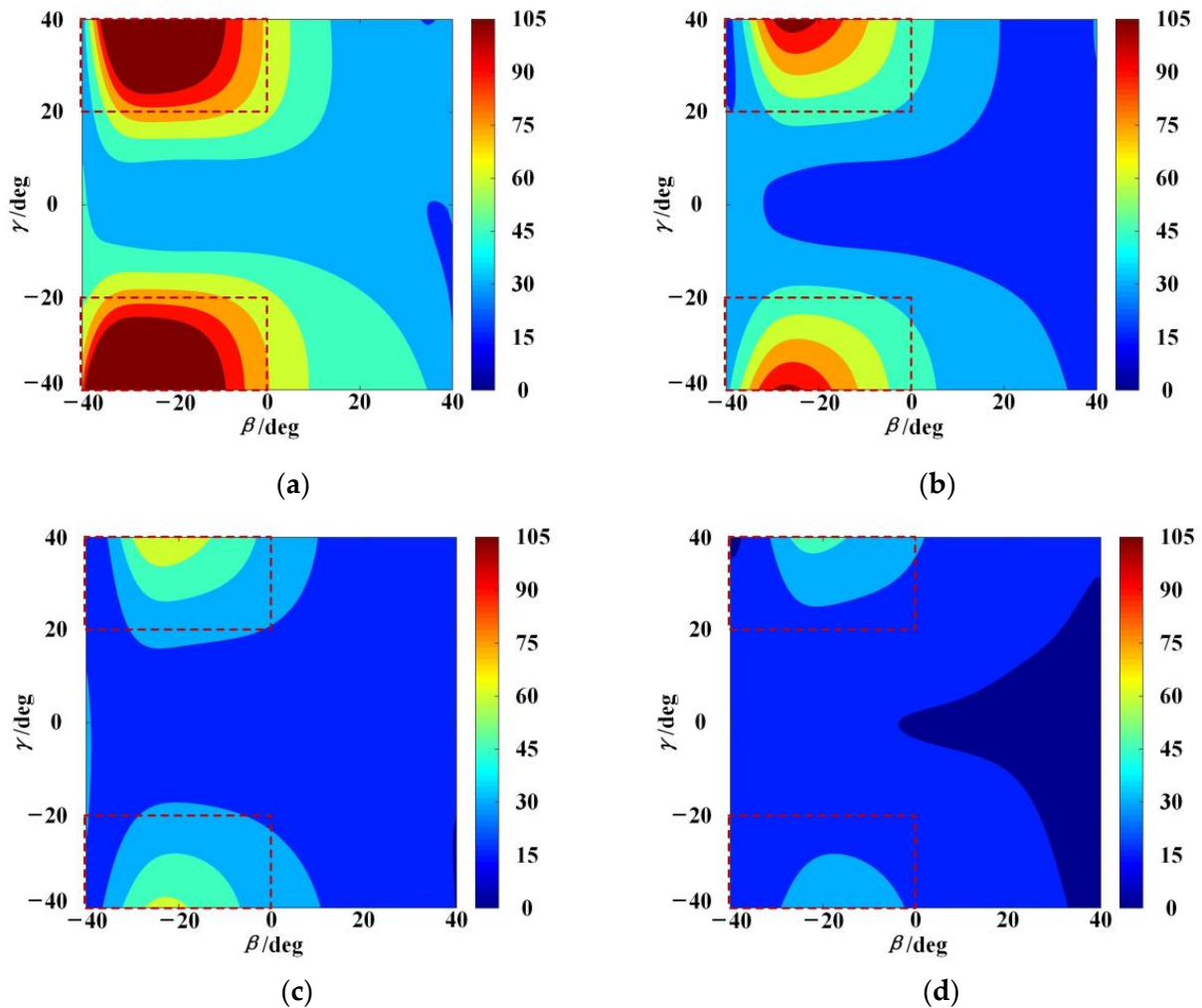
Figure 9. Influence of operational height on the distributions of κ in the orientation workspace when $W_M = \begin{bmatrix} 100\,\text{N} & 100\,\text{N} & 100\,\text{N} & 100\,\text{Nm} & 100\,\text{Nm} & 100\,\text{Nm} \end{bmatrix}$: (**a**) $z_o = 450$ mm; (**b**) $z_o = 550$ mm; (**c**) $z_o = 650$ mm; (**d**) $z_o = 750$ mm.

Table 4. Minimum, maximum, and average values of stiffness index in the selected and other orientation ranges with different operational heights.

Operational Height z_o (mm)	Orientation Ranges	Minimum Value (J^{-1})	Maximum Value (J^{-1})	Average Value (J^{-1})
	Selected ranges	32.3846	206.2666	106.9120
450	Other ranges	28.8323	79.9983	43.6147
	Relative proportion	112.32%	257.84%	245.13%

Table 4. *Cont.*

Operational Height z_o (mm)	Orientation Ranges	Minimum Value (J^{-1})	Maximum Value (J^{-1})	Average Value (J^{-1})
550	Selected ranges	21.2057	114.0750	63.0326
	Other ranges	19.9371	51.4777	30.5014
	Relative proportion	106.36%	221.60%	206.65%
650	Selected ranges	16.1296	73.4454	40.4478
	Other ranges	14.5746	39.3239	22.6852
	Relative proportion	110.67%	186.77%	178.30%
750	Selected ranges	13.2386	50.0849	27.8131
	Other ranges	11.1325	30.6698	17.5839
	Relative proportion	118.92%	163.30%	158.17%

5. Conclusions

This paper establishes the elastostatic stiffness model of the redundantly actuated 2UPR–2PRU PM in the analytical form, including the limb stiffness models and overall stiffness model. Based on the principle of the strain energy, the expression of actuation and constraint wrenches, the strain energy in the limb, and the deformations along the direction of each wrench are successively derived in this paper, and then the analytical expressions of the stiffness matrices are obtained. All the results in the stiffness analysis have intuitive forms of expression and clear physical meanings, which can provide references for actual applications. Comparable results of numerical examples with ANSYS show that all the relative errors of the deformations in the three cases with small deformations are less than 0.67%, and all the relative errors of the deformations in the case with large deformations are less than 3.52%; these results verify the correctness and universality of the stiffness model of 2UPR–2PRU PM. The stiffness index based on energy is adopted to evaluate the stiffness performance under different external loads. Using this stiffness index, the performance in singular configurations can also be measured. In addition, this index can also provide good guidance for the selection of workspaces with better performance. Based on the above foundation, our future work will focus on the extension of the stiffness model, such as the establishment of a complete stiffness model that takes the compliance of joints, links, and the end-effector and the influence of frictional effect into account. The links in the limbs will not be assumed with a uniform cross-section. The area, effective shear area, area moment of the inertia, and polar moment of the inertia of the cross-section will not be constant. Error modeling, trajectory planning, and control will also be focused on in the future.

Author Contributions: Methodology, X.C. and L.X.; software, L.X.; validation, X.C., W.Y. and L.X.; data curation, X.C.; writing—original draft preparation, X.C. and L.X.; writing—review and editing, X.C., W.Y., L.X. and Q.L.; supervision, Q.L. All authors have read and agreed to the published version of the manuscript.

Data Availability Statement: Not applicable.

Conflicts of Interest: The authors declare no conflict of interest.

References

1. Kim, J.; Park, F.C.; Ryu, S.J.; Kim, J.; Hwang, J.C.; Park, C.; Iurascu, C.C. Design and analysis of a redundantly actuated parallel mechanism for rapid machining. *IEEE Trans. Robot. Autom.* **2001**, *17*, 423–434. [CrossRef]
2. Wang, L.P.; Wu, J.; Wang, J.S.; You, Z. An experimental study of a redundantly actuated parallel manipulator for a 5-DOF hybrid machine tool. *IEEE/ASME Trans. Mechatron.* **2009**, *14*, 72–81. [CrossRef]
3. Xu, L.M.; Chai, X.X.; Li, Q.C.; Zhang, L.A.; Ye, W. Design and experimental investigation of a new 2R1T overconstrained parallel kinematic machine with actuation redundancy. *J. Mech. Robot.* **2019**, *11*, 031016. [CrossRef]

4. Gosselin, C.; Schreiber, L.T. Redundancy in parallel mechanisms: A review. *Appl. Mech. Rev.* **2018**, *70*, 010802. [CrossRef]
5. Lee, M.; Jeong, H.; Lee, D. Design optimization of 3-DOF redundant planar parallel kinematic mechanism based finishing cut stage for improving surface roughness of FDM 3D printed sculptures. *Mathematics* **2021**, *9*, 961. [CrossRef]
6. Shen, X.D.; Xu, L.M.; Li, Q.C. Motion/force constraint indices of redundantly actuated parallel manipulators with over constraints. *Mech. Mach. Theor.* **2021**, *165*, 104427. [CrossRef]
7. Siciliano, B.; Khatib, O. *Handbook of Robotics*; Springer: Berlin/Heidelberg, Germany, 2008.
8. EI-Khasawneh, B.S.; Ferreira, P.M. Computation of stiffness and stiffness bounds for parallel link manipulators. *Int. J. Mach. Tools Manuf.* **1999**, *39*, 321–342. [CrossRef]
9. Corradini, C.; Fauroux, J.; Krut, S.; Company, O. Evaluation of a 4-degree of freedom parallel manipulator stiffness. In Proceedings of the 11th World Congress in Mechanisms and Machine Science, Tianjin, China, 18–21 August 2003; pp. 1857–1861.
10. Bouzgarrou, B.; Fauroux, J.; Gogu, G.; Heerah, Y. Rigidity analysis of T3R1 parallel robot with uncoupled kinematics. In Proceedings of the 35th International Symposium on Robotics, Paris, France, 23–26 March 2004; pp. 1–6.
11. Rizk, R.; Fauroux, J.C.; Munteanu, M.; Gogu, G. A comparative stiffness analysis of a reconfigurable parallel machine with three or four degrees of mobility. *J. Mach. Eng.* **2006**, *6*, 45–55.
12. Klimchik, A.; Pashkevich, A.; Chablat, D. CAD-based approach for identification of elasto-static parameters of robotic manipulators. *Finite Elem. Anal. Des.* **2013**, *75*, 19–30. [CrossRef]
13. Pashkevich, A.; Chablat, D.; Wenger, P. Stiffness analysis of overconstrained parallel manipulators. *Mech. Mach. Theor.* **2009**, *44*, 966–982. [CrossRef]
14. Klimchik, A.; Chablat, D.; Pashkevich, A. Stiffness modeling for perfect and non-perfect parallel manipulators under internal and external loadings. *Mech. Mach. Theor.* **2014**, *79*, 1–28. [CrossRef]
15. Lončarič, J. Normal forms of stiffness and compliance matrices. *IEEE J. Robot. Autom.* **1987**, *3*, 567–572. [CrossRef]
16. Gosselin, C. Stiffness mapping for parallel manipulators. *IEEE Trans. Robot. Autom.* **1990**, *6*, 377–382. [CrossRef]
17. Gosselin, C.; Zhang, D. Stiffness analysis of parallel mechanisms using a lumped model. *Int. J. Robot. Autom.* **2002**, *17*, 17–27.
18. Zhang, D.; Xi, F.F.; Mechefske, C.M.; Lang, S.Y. Analysis of parallel kinematic machine with kinetostatic modelling method. *Robot. Comput.-Integr. Manuf.* **2004**, *20*, 151–165. [CrossRef]
19. Xi, F.F.; Zhang, D.; Mechefske, C.M.; Lang, S.Y. Global kinetostatic modelling of tripod-based parallel kinematic machine. *Mech. Mach. Theor.* **2004**, *39*, 357–377. [CrossRef]
20. Ciblak, N.; Lipkin, H. Asymmetric Cartesian stiffness for the modelling of compliant robotic systems. In Proceedings of the ASME 1994 Design Technical Conferences collocated with the ASME 1994 International Computers in Engineering Conference and Exhibition and the ASME 1994 8th Annual Database Symposium, Minneapolis, MN, USA, 11–14 September 1994; pp. 197–204.
21. Žefran, M.; Kumar, V. Affine connections for the Cartesian stiffness matrix. In Proceedings of the 1997 IEEE International Conference on Robotics and Automation, Albuquerque, NM, USA, 20–25 April 1997; pp. 1376–1381.
22. Howard, S.; Žefran, M.; Kumar, V. On the 6×6 Cartesian stiffness matrix for three-dimensional motions. *Mech. Mach. Theor.* **1998**, *33*, 389–408. [CrossRef]
23. Žefran, M.; Kumar, V. Coordinate-free formulation of the cartesian stiffness matrix. In *Recent Advances in Robot Kinematics*; Springer: Dordrecht, The Netherlands, 1996; pp. 119–128.
24. Alici, G.; Shirinzadeh, B. Enhanced stiffness modeling, identification and characterization for robot manipulators. *IEEE Trans. Robot.* **2005**, *21*, 554–564. [CrossRef]
25. Kövecses, J.; Angeles, J. The stiffness matrix in elastically articulated rigid-body systems. *Multibody Syst. Dyn.* **2007**, *18*, 169–184. [CrossRef]
26. Portman, V.T. Stiffness evaluation of machines and robots: Minimum collinear stiffness value approach. *J. Mech. Robot.* **2011**, *3*, 011015. [CrossRef]
27. Portman, V.T. Robot stiffness evaluability problem: Solution by Schur complements and collinear stiffness values. *Mech. Mach. Theor.* **2021**, *161*, 104297. [CrossRef]
28. Taghvaeipour, A.; Angeles, J.; Lessard, L. On the elastostatic analysis of mechanical systems. *Mech. Mach. Theor.* **2012**, *58*, 202–216. [CrossRef]
29. Ding, J.Z.; Wang, C.J.; Wu, H.Y. Accuracy analysis of redundantly actuated and overconstrained parallel mechanisms with actuation errors. *J. Mech. Robot.* **2018**, *10*, 061010. [CrossRef]
30. Cao, W.A.; Ding, H.F.; Yang, D.H. A method for compliance modeling of five degree-of-freedom overconstrained parallel robotic mechanisms with 3T2R output motion. *J. Mech. Robot.* **2017**, *9*, 011011. [CrossRef]
31. Yu, G.; Wang, L.P.; Wu, J.; Wang, D.; Hu, C.J. Stiffness modeling approach for a 3-DOF parallel manipulator with consideration of nonlinear joint stiffness. *Mech. Mach. Theor.* **2018**, *123*, 137–152. [CrossRef]
32. Xu, L.M.; Li, Q.C.; Zhang, N.B.; Chen, Q.H. Mobility, kinematic analysis, and dimensional optimization of new three-degrees-of-freedom parallel manipulator with actuation redundancy. *J. Mech. Robot.* **2017**, *9*, 041008. [CrossRef]
33. Yang, C.; Li, Q.C.; Chen, Q.H.; Xu, L.M. Elastostatic stiffness modeling of overconstrained parallel manipulators. *Mech. Mach. Theor.* **2018**, *122*, 58–74. [CrossRef]
34. Yan, S.J.; Ong, S.K.; Nee, A.Y.C. Stiffness analysis of parallelogram-type parallel manipulators using a strain energy method. *Robot. Comput.-Integr. Manuf.* **2016**, *37*, 13–22. [CrossRef]

35. Enferadi, J.; Tootoonchi, A.A. Accuracy and stiffness analysis of a 3-RRP spherical parallel manipulator. *Robotica* **2011**, *29*, 193–209. [CrossRef]

36. Rezaei, A.; Akbarzadeh, A.; Akbarzadeh, T.M. An investigation on stiffness of a 3-PSP spatial parallel mechanism with flexible moving platform using invariant form. *Mech. Mach. Theor.* **2012**, *51*, 195–216. [CrossRef]

37. Rezaei, A.; Akbarzadeh, A. Position and stiffness analysis of a new asymmetric 2PRR–PPR parallel CNC machine. *Adv. Robot.* **2013**, *27*, 133–145. [CrossRef]

38. Xu, Y.D.; Yao, J.T.; Jin, L.R.; Zhao, Y.S. Method for force analysis of the overconstrained parallel mechanism considering the link's spatial composite elastic deformations. *J. Mech. Eng.* **2015**, *51*, 53–60. [CrossRef]

39. Courteille, E.; Deblaise, D.; Maurine, P. Design optimization of a Delta-like parallel robot through global stiffness performance evaluation. In Proceedings of the 2009 IEEE/RSJ International Conference on Intelligent Robots and Systems, Saint Louis, MO, USA, 10–15 October 2009; pp. 5159–5166.

40. Carbone, G.; Ceccarelli, M. Comparison of indices for stiffness performance evaluation. *Front. Mech. Eng. China* **2010**, *5*, 270–278. [CrossRef]

41. Angeles, J. On the nature of the Cartesian stiffness matrix. *Ing. Mec.* **2010**, *3*, 163–170.

42. Wu, G.; Zou, P. Stiffness analysis and comparison of a Biglide parallel grinder with alternative spatial modular parallelograms. *Robotica* **2017**, *35*, 1310–1326. [CrossRef]